Journal of Controlled Release 363 (2023) 747–755

Contents lists available at ScienceDirect

Journal of Controlled Release

journal homepage: www.elsevier.com/locate/jconrel

Dependence of sonoporation efficiency on microbubble size: An in vitro monodisperse microbubble study

Benjamin van Elburg [a,1], Joke Deprez [b,1], Martin van den Broek [d], Stefaan C. De Smedt [b,c], Michel Versluis [a], Guillaume Lajoinie [a], Ine Lentacker [b,c], Tim Segers [d,*]

[a] Physics of Fluids Group and Technical Medical (TechMed) Center, University of Twente, Enschede, the Netherlands
[b] Laboratory of General Biochemistry and Physical Pharmacy, Ghent Research Group on Nanomedicine, Ghent University, Ghent, Belgium
[c] Cancer Research Institute Ghent (CRIG), Ghent, Belgium
[d] BIOS / Lab on a Chip Group, Max-Planck Center Twente for Complex Fluid Dynamics, MESA+ Institute for Nanotechnology, University of Twente, Enschede, Netherlands

ARTICLE INFO

Keywords:
Sonoporation
Monodisperse microbubbles
Therapy
Ultrasound
Ultrasound contrast agents

ABSTRACT

Sonoporation is the process where intracellular drug delivery is facilitated by ultrasound-driven microbubble oscillations. Several mechanisms have been proposed to relate microbubble dynamics to sonoporation including shear and normal stress. The present work aims to gain insight into the role of microbubble size on sonoporation and thereby into the relevant mechanism(s) of sonoporation. To this end, we measured the sonoporation efficiency while varying microbubble size using monodisperse microbubble suspensions. Sonoporation experiments were performed in vitro on cell monolayers using a single ultrasound pulse with a fixed frequency of 1 MHz while the acoustic pressure amplitude and pulse length were varied at 250, 500, and 750 kPa, and 10, 100, and 1000 cycles, respectively. Sonoporation efficiency was quantified using flow cytometry by measuring the FITC-dextran (4 kDa and 2 MDa) fluorescence intensity in 10,000 cells per experiment to average out inherent variations in the bioresponse. Using ultra-high-speed imaging at 10 million frames per second, we demonstrate that the bubble oscillation amplitude is nearly independent of the equilibrium bubble radius at acoustic pressure amplitudes that induce sonoporation ($\geq$ 500 kPa). However, we show that sonoporation efficiency is strongly dependent on the equilibrium bubble size and that under all explored driving conditions most efficiently induced by bubbles with a radius of 4.7 μm. Polydisperse microbubbles with a typical ultrasound contrast agent size distribution perform almost an order of magnitude lower in terms of sonoporation efficiency than the 4.7-μm bubbles. We elucidate that for our system shear stress is highly unlikely the mechanism of action. By contrast, we show that sonoporation efficiency correlates well with an estimate of the bubble-induced normal stress.

1. Introduction

Ultrasound-driven volumetric microbubble oscillations can induce transient cell membrane permeabilization enabling the otherwise obstructed transmembrane delivery of novel therapeutics such as gene constructs, antibodies, and nanomedicines directly to the cytoplasm of living cells [1–4]. In this emerging therapeutic paradigm, controlled uptake by sonoporation is facilitated by intravenously injected microbubbles. Besides their therapeutic effect, ultrasound-driven microbubbles produce a strong nonlinear echo that allows concurrent diagnostic ultrasound imaging of their location and cavitation activity [5]. As such, microbubbles may become theranostic tools enabling spatiotemporally-controlled drug and gene delivery via sonoporation.

Over the past decades, several mechanisms of sonoporation have been proposed. These include oscillatory normal stress due to (i) the mechanical palpation and invagination of the microbubble wall on the cell membrane [6,7], and (ii) due to the primary and secondary acoustic radiation forces [1,8]. Considerable attention has also been given to (iii) shear stress due to both steady and non-steady bubble-induced fluid microstreaming [9–13]. Additionally, sonoporation can be induced by (iv) high-speed fluid microjets ($\mathcal{O}$(100) m/s) generated by the inertial collapse of a bubble [14–16]. Due to the complexity of the coupled

* Corresponding author at: BIOS / Lab-on-a-Chip Group, University of Twente, Postbus 217, Enschede 7500 AE, the Netherlands.
E-mail address: t.j.segers@utwente.nl (T. Segers).
[1] These authors contributed equally to this work.

https://doi.org/10.1016/j.jconrel.2023.09.047
Received 12 May 2023; Received in revised form 24 July 2023; Accepted 26 September 2023
Available online 21 October 2023

physics, biophysics, and biology of sonoporation, the relevance of the proposed mechanisms and their dependence on bubble dynamics remain poorly understood [17,18]. So far and irrespective of the underlying mechanisms, sonoporation has often been thought to be governed by the bubble oscillation amplitude [11,19,20] where low oscillation amplitudes can be insufficient to induce sonoporation while high amplitudes can induce cell death and tissue damage [21].

The oscillation amplitude of a microbubble is mainly governed by the combination of the bubble radius R_0 and the ultrasound driving frequency and acoustic pressure [23]. At acoustic pressure amplitudes typically lower than those used to induce sonoporation ($\lesssim$ 150 kPa), bubble dynamics is governed by a resonance behavior (black curve in Fig. 1) with the characteristic Minnaert resonance frequency f_0 extracted from $f_0 \cdot R_0 \approx 3.3$ μm · MHz [24]. At higher acoustic pressure amplitudes, the bubble dynamics becomes highly nonlinear and less governed by resonance. This is demonstrated by Rayleigh-Plesset type modeling of a coated bubble driven by 1-MHz ultrasound, which predicts a very similar amplitude of oscillation for bubbles with radii ranging from 2 to 8 μm when the acoustic pressure amplitude is 250 kPa or higher, see Fig. 1 [22]. Quantification of the sonoporation efficiency of microbubbles of a different size but oscillating at a similar amplitude of oscillation may gain insight into the relevant mechanisms of sonoporation. The aim of the present work is therefore to address the question: what is the dependence of sonoporation efficiency on the microbubble size?

Hitherto, only polydisperse ultrasound contrast agent (UCA) microbubbles have been used for sonoporation, which were designed more than three decades ago for diagnostic organ perfusion imaging [25]. The radii of UCA bubbles typically range from 0.5 to 5 μm. Conversely, monodisperse microbubbles can be formed by microfluidic flow-focusing [26–29]. In a flow focusing device, a gas thread is focused between a liquid co-flow through a narrow orifice where it pinches off to release monodisperse bubbles. Recent advances in lipid-coated bubble production by flow-focusing allow the formation of size-controlled and highly stable monodisperse microbubble suspensions [29–36].

Besides the ultrasound frequency and pressure, the driving pulse length is also a control parameter in sonoporation therapy. A wide range of pulse lengths have been employed to induce sonoporation, i.e., from a single pulse of a few acoustic cycles [11,20,37] to many repetitions of pulses containing thousands of cycles [38–42]. In in vitro sonoporation experiments on cell monolayer substrates, microbubbles driven by long

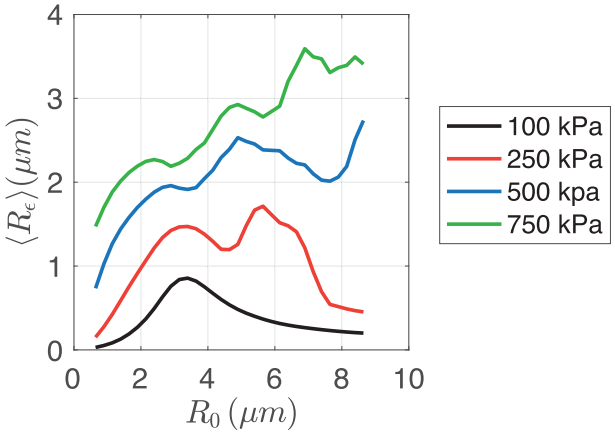

Fig. 1. Modeled oscillation amplitude $\langle R_\epsilon \rangle = \frac{1}{2}(R_{max} - R_{min})$ averaged over the 16 cycles of the employed 1 MHz driving pulse, of which the pressure amplitude was varied at 100, 250, 500, and 750 kPa. The results were obtained by solving a Rayleigh-Plesset type model for a coated bubble [22] using a typical shell properties (shell stiffness of 0.5 N/m, shell viscosity of 1×10^{-8} kg/s, and initial surface tension of 20 mN/m). Note that the characteristic resonance behavior of a microbubble (black curve) disappears when the acoustic driving pressure amplitude is increased beyond 100 kPa.

ultrasound pulses will cluster due to the acoustic secondary radiation force [43]. Such clustering directly affects the oscillation dynamics of the bubbles [44]. Ultrasound-driven bubble oscillations during prolonged insonation are also most likely affected by bubble size changes, e.g., growth due to bubble coalescence, by rectified diffusion, or dissolution [45,46]. Furthermore, bubble dissolution during the time between two successive insonation pulses will most likely be enhanced by lipid shedding during the previous driving pulse [47–49]. Thus, correlating sonoporation efficiency to microbubble size and the corresponding microbubble dynamics requires the use of single ultrasound driving pulses ideally with a limited number of cycles.

Sonoporation efficiency can be measured by quantifying the fluorescence intensity of a model drug diffused into cells post ultrasound treatment [50,51]. To this end, two experimental approaches exist. First, optical (confocal) microscopy can be used. It can furthermore be combined with ultra-high-speed imaging to simultaneously characterize the bubble dynamics and its effect on a nearby cell layer [6,11,19,52–54]. However, data are typically sparse and scattered and largely inconclusive because bubble-cell interactions are prone to a large variability, owing to the cell biology statistics itself and, potentially, to the local positioning of the bubble with respect to the target cell. Also, in confocal imaging, the number of cells that can be characterized is limited to $\mathscr{O}(100)$ per study due to the delicate and time consuming nature of the experiments. The second approach, which is followed in the present work, is flow cytometry. Flow cytometry can discriminate drug uptake through sonoporation from that by endocytosis (internalization of membrane vesicles) [39,55]. The major advantage of flow cytometry is that it can be used to measure the fluorescence intensity of thousands of cells within minutes. Thereby, flow cytometry has great potential for mechanistic sonoporation studies, in combination with monodisperse bubbles with a uniform acoustic response, to average out the inherent variations in bubble-cell interactions.

In this work, we combine the use of monodisperse microbubble suspensions, flow cytometry, and ultra-high-speed imaging at 10 million frames per second, to reveal the dependence of sonoporation efficiency on microbubble size and the resulting bubble dynamics. Furthermore, the sonoporation results are compared to those obtained with a polydisperse bubble suspension. Thereby, we aim to gain further insight into the mechanisms of sonoporation. The paper is organized as follows. We start by describing the materials employed for bubble production and cell cultures, and the methods to quantify sonoporation efficiency. Subsequently, we present our results and discussions. Finally, we discuss potential mechanisms of sonoporation by comparing their scaling behavior with bubble size to the measured sonoporation efficiency. We end the paper with conclusions.

2. Materials and methods

2.1. Microbubble formation and characterization

Monodisperse microbubble suspensions were produced using the flow-focusing device shown in Fig. 2A, which is described in detail in [56]. The gas and liquid flows were controlled using pressure and mass-flow controllers [57]. The temperature during bubble formation was kept at 60 °C to minimize bubble coalescence in the outlet of the flow-focusing device [35]. The lipid coating material comprised DSPC mixed with DPPE-PEG5000 at a 9:1 molar ratio (Corden Pharma, Liestal, Switzerland). The total lipid concentration was 12.5 mg per mL of air-saturated Isoton (Beckman Coulter Life Sciences, Indianapolis, IN, USA). The lipid dispersion was prepared exactly as described by [34]. The freshly formed bubbles were initially filled with a gas mixture of 15 v% C_4F_{10} in CO_2 (*v*/v) to minimize foam formation [36] through Ostwald ripening [33]. The size distributions (Fig. 2B) were characterized using a Coulter Counter (Beckman Coulter Life Sciences, Indianapolis, IN, USA).

The employed polydisperse bubble suspension (Fig. 2B) was

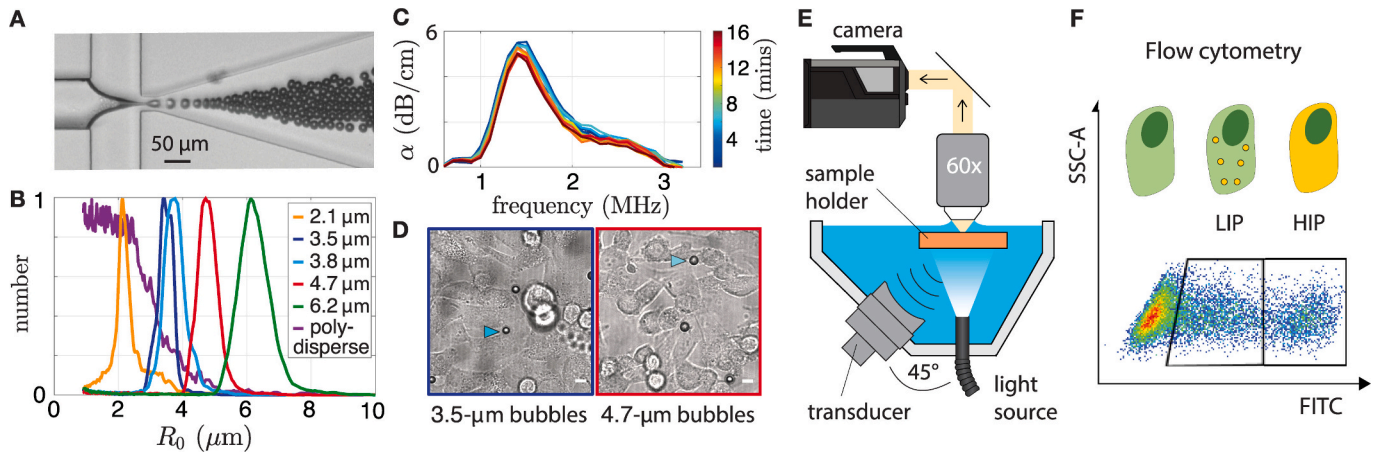

Fig. 2. (A) Monodisperse microbubble suspensions were formed in a flow-focusing device. (B) Size distributions of the employed bubble suspensions. (C) Attenuation α spectra of the bubbles diluted in cell medium at 37 °C measured every minute over the course of 16 min. The equality of the spectra demonstrates that the bubbles are highly stable under the conditions during the sonoporation experiments. (D) The bubbles (blue arrows) were left to float against a confluent cell layer (scale bar 10 μm) where (E) they were insonified by a single ultrasound pulse at a frequency of 1 MHz. (F) After insonation, the cell layer was left to incubate for 10 min after which it was further processed by flow cytometry. The low FITC-intensity population (LIP) corresponds to FITC-dextran uptake via endocytosis and the high-intensity population (HIP) to that via sonoporation [39]. (For interpretation of the references to colour in this figure legend, the reader is referred to the web version of this article.)

produced using the same lipid mixture, only diluted 20 times using Isoton (0.63 mg/mL) to a typical concentration that can be used to form polydisperse bubbles by mechanical agitation using a Capmix device (3M-ESPE, Diegem, Belgium). To this end, 1 mL of lipid mixture contained in a 2 mL vial with a pure C_4F_{10} headspace was mechanically agitated for 15 s.

The microbubble suspensions were highly diluted in an air-saturated cell medium kept at a temperature of 37 °C for approximately 7 mins before being insonified in the sonoporation experiments, which may affect their size distribution. Therefore, microbubble stability in cell medium was characterized over time. To this end, narrowband (30 cycles) attenuation curves were measured as described in [58], once per minute for a total duration of 16 mins at a peak negative acoustic pressure amplitude of 50 kPa. It was found that, during the entire 16 mins, the frequency of maximum attenuation (microbubble resonance frequency) did not change for bubbles in cell medium at 37 °C (Fig. 2C) demonstrating their size and acoustic stability over the course of the sonoporation experiments (prior to insonation).

2.2. Cell culture

Bowes Lung Metastases (BLM) melanoma cells were grown in culture flasks in a humidified atmosphere with 5% CO_2 at 37 °C. The culture medium was Dulbecco's Modified Eagle Medium with Nutrient Mixture F12 (Gibco, Merelbeke, Belgium), supplemented with 10% (*v*/v) fetal bovine serum (FBS) (Hyclone, Thermo Scientific, MA, USA), 20 U/mL penicillin–streptomycin (Gibco, Merelbeke, Belgium), 2 mM L-glutamine (Gibco, Merelbeke, Belgium) and 10 mM HEPES (4-(2-hydroxyethyl)-1-piperazineethanesulfonic acid) (Sigma-Aldrich, Diegem, Belgium). The viscosity of the cell medium was 1 mPa·s (37 °C) [59]. One day before the experiment, cells were harvested by 0.05% trypsin-EDTA (Ethylenediaminetetraacetic acid) (Gibco, Merelbeke, Belgium) and reseeded in Lumox dishes (Sarstedt AG & Co. KG, Nümbrecht, Germany) at a density of 5×10^5 cells per Lumox dish, reaching confluency after 24 h.

2.3. Sonoporation efficiency characterization

The Lumox dishes were sealed with an ultrasound-transparent film mounted within a 3D-printed lid. Subsequently, the cell medium was replaced by a mixture of cell-medium, microbubbles, and (fluorescein isothiocyanate)-dextrans (FITC-dextrans)(Sigma-Aldrich, Diegem, Belgium, excitation/emission maxima: 490/520 nm, resp.) with a molecular weight of 4 kDa or 2 MDa (estimated radius of 1.23 nm and 32.78 nm, resp. [60]), to discriminate between small and large pore formation. The FITC-dextran concentrations were 0.25 mg/mL and 5 mg/mL, for the 4 kDa or 2 MDa molecular weights, respectively. The microbubbles were diluted to approximately 1 bubble per 15 cells (Fig. 2D) to minimize ultrasound-induced bubble-bubble interactions, which are beyond the scope of this study. After microbubble injection, the dish was turned upside-down and placed in a temperature controlled (37 °C) incubator for 5 min to allow the microbubbles to float up against the cell layer. Considering the total time between injection and ultrasound exposure, all microbubbles will then have reached the cell layer. The Lumox dish was then kept in upside-down position and placed in a 37 °C water tank where it was exposed to ultrasound.

The bubbles were always insonified by a single 1-MHz ultrasound pulse. The ultrasound transmit pulses were generated with an arbitrary waveform generator (model 8026, Tabor Electronics, Tel Hanan, Israel), amplified by a power amplifier (50 dB, 350 L, Electronics and Innovation, Rochester, USA), and transmitted by an unfocused, single-element immersion transducer with a center frequency of 1 MHz (C302-SU, Olympus, Berchem, Belgium). The transducer was mounted at a side of a water tank at a 45° angle with respect to the vertical, and at a standoff distance of approximately 8 cm to the cell monolayer in the Lumox dish (Fig. 2E). This standoff distance was deliberately chosen to be larger than the natural focus of the transducer. As such, the area of constant acoustic insonation pressure (within ≈ –4 dB, see supplementary information) was larger than the 1 cm diameter circle of the Lumox dish that was used for further processing, see also next paragraph. The acoustic output of the transducer was measured using a calibrated needle hydrophone (0.24-mm-diameter, Precision Acoustics, Dorset, UK). Brightfield imaging, before and after the sonoporation experiments, was performed using a confocal microscope (Yokogawa CSU-X, Nikon, Amsterdam, The Netherlands) with a 60× water-immersion objective (NIRApo, 1.0 NA, Nikon). An objective inverter (LSM TECH, Wellsville, USA) was used to position the objective on top of the Lumox dish. The focal plane of the objective was co-aligned with the natural focus of the transducer using the hydrophone. During ultrasound insonation, the objective was moved out of the water to avoid ultrasound reflections from its surface. All acoustic pressures reported are peak negative pressure (PNP) amplitudes.

After insonation, the Lumox dish was placed back into the incubator

for 10 min to allow the model drug to diffuse into porated cells, and to allow them to recover. Subsequently, the exposed area with a diameter of 1 cm was cut out with a scalpel. The cells were then harvested from the cut-out membrane using 0.05% trypsin-EDTA (ethylenediaminetetraacetic acid) (Gibco, Merelbeke, Belgium) to obtain freely floating cells in suspension. The subsequent flow cytometry procedure is described in detail in [39] and in the Supplementary information. In short, the harvested cells were stained with the 7-AAD viability dye (Thermo Fisher Scientific, Waltham, WA, USA). The samples were then characterized using a benchtop flow cytometer (Cytoflex, Beckman Coulter) until a total cell count of 10.000 was reached. The obtained data was analyzed (Fig. 2F) using the FlowJo software (BD company). Control measurements were performed using the same procedure, without exposure to ultrasound. Gating of the fluoresence intensity levels discriminates between two populations: the low intensity population (LIP) represents cells with drug uptake through endocytosis and the high intensity population (HIP) represents cells with drug uptake through sonoporation [39]. The endocytosis and sonoporation efficiency percentages are defined as the fraction of endocytic or sonoporated cells out of the group of viable cells. At each ultrasound setting and for each bubble size distribution, at least 3 experiments were performed such that the standard error of the mean could be determined.

2.4. Ultra-high-speed imaging of bubble dynamics

To gain insight into the relation between sonoporation efficiency, bubble size, and bubble dynamics, the radius–time ($R(t)$) curves of the polydisperse microbubbles were recorded using ultra-high-speed imaging at 10 million frames/s (Shimadzu HPV-X2). The bubbles were again left to float against the cell layer on the Lumox dish were they were driven by a single 1-MHz, 10-cycle ultrasound pulse at a PNP of 100 kPa or 500 kPa. The bubble radius was extracted from each frame of the high-speed movies by a semi-automated image analysis algorithm programmed in MATLAB (The Mathworks, Natick, MA). The bubble radius was measured from the inflection point on the intensity profile of the brightfield image of the bubble [61]. The average oscillation amplitude $\langle R_\epsilon \rangle$ was obtained from the $R(t)$ curves and defined as follows: $\langle R_\epsilon \rangle = (R_{max} - R_{min})/2$, with R_{max} the average of the maxima of the $R(t)$ curves and R_{min} the average of the minima of the $R(t)$ curves, where only local minima and maxima within at least 20% of the maximum amplitude where taken into account to capture only the dynamics of the bubbles during ultrasound driving.

To gain insight into the role of bubble translation, coalescence, and dissolution during 1000-cycle driving pulses, a second high-speed imaging experiment was performed at 200,000 frames/s. The insonation frequency and pressure were 1 MHz and 500 kPa, respectively. Imaging was performed on microbubbles floating against a flat and soft 50-μm thick polyacrylamide hydrogel. The bubble concentration was identical to that used in the sonoporation experiments. The hydrogel, prepared as in [62], was chosen to mimic the presence of the compliant cell layer. Its shear modulus compares well to that of spleen and kidney tissue [63].

3. Results and discussions

3.1. Ultrasound-driven dynamics of microbubbles floating against the cell layer

The measured amplitude of oscillation $\langle R_\epsilon \rangle$ of microbubbles floating against the cell layer is plotted in Fig. 3. Fig. 3A shows $\langle R_\epsilon \rangle$ measured at a PNP of 100 kPa and Fig. 3B that at a PNP of 500 kPa. As expected from Fig. 1, a resonance behavior is observed for bubbles driven at a PNP of 100 kPa whereas at a PNP of 500 kPa the resonance behavior disappears. The resonant bubble radius measured at a PNP of 100 kPa ($\approx$ 3.5 μm) is close to that predicted by the Minneart frequency: $f_0 \times R_0 \approx 3.3$ μm MHz. For reference, the $\langle R_\epsilon \rangle$ curves predicted by a Rayleigh-Plesset (RP) type equation for a coated bubble from Fig. 1 are also plotted in Fig. 3 (solid curves). Even though the RP equation is only valid for a bubble in the unbounded fluid [22,64], the agreement with the measured $\langle R_\epsilon \rangle$ of the microbubbles floating against the cell layer is surprisingly good. The spread in the measured $\langle R_\epsilon \rangle$ at a PNP of 500 kPa most likely originates from the variation in the local position of the bubble with respect to the target cell(s) and the complex often non-spherical interaction of the inertially cavitating bubbles with the compliant cell layer [49,65–68]. Nevertheless, on average, the measurements show that the oscillation amplitude of bubbles driven at an ultrasound frequency of 1 MHz and a PNP of 500 kPa is very similar across bubble radii ranging from 2 to 8 μm.

3.2. Sonoporation experiments

First, the roles of the PNP and pulse length on endocytosis and sonoporation efficiency were studied for two bubble populations (3.5 μm and 4.7 μm radius, Fig. 2B) to select the ultrasound driving

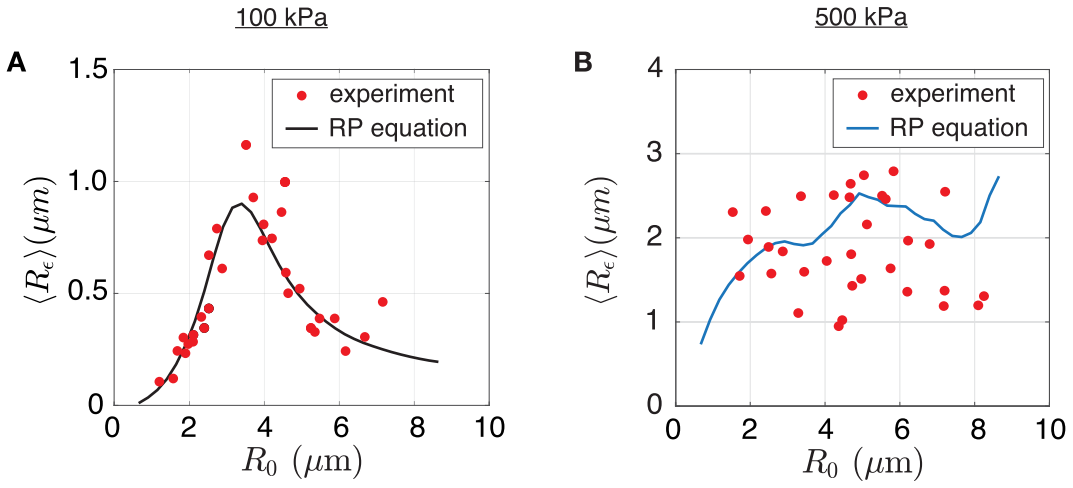

Fig. 3. Measured amplitude of oscillation $\langle R_\epsilon \rangle$ (red dots) averaged over the 10-cycle driving pulse and plotted as a function of the equilibrium microbubble radius R_0. The microbubbles were floating against the cell layer. The solid lines show $\langle R_\epsilon \rangle$ obtained by numerically solving a Rayleigh-Plesset type equation for a coated bubble ($\chi = 0.5$ N/m, $\kappa_s = 1 \times 10^{-8}$, $\sigma(R_0) = 20$ mN/m). The amplitude of oscillation measured at a PNP of 100 kPa is shown in (A) and that at a PNP of 500 kPa in (B). Note that the narrowband resonance behavior as observed in (A) disappears when the acoustic pressure is increased from 100 kPa to 500 kPa, see (B). (For interpretation of the references to colour in this figure legend, the reader is referred to the web version of this article.)

parameters for the sonoporation measurements using all size distributions. The employed PNPs and pulse lengths were 250 and 500 kPa and 10, 100 and 1000 cycles, respectively. The measured endocytosis and sonoporation efficiencies are shown in Fig. 4. The control data is presented in Figs. 4 A and D. Both figures show control data measured without FITC dextran (indicated by "no FITC"), with 2 MDa FITC dextran but without ultrasound and microbubbles (indicated by "no US"), and with 2 MDa FITC dextran and microbubbles, but no ultrasound (indicated by "no US, with MBs"). The maximum percentage of endocytic cells in the control groups is represented by the horizontal dotted line. Efficiency values below the dotted lines thus cannot be attributed to ultrasound-driven bubble dynamics. Similarly, the dotted lines in Figs. 4D and F represent the highest percentage of sonoporated cells in the control groups.

Regarding endocytosis (Figs. 4B and C), in all experiments with bubbles and ultrasound the percentage of endocytosis exceeds the control value. This confirms previous findings that oscillating microbubbles can increase endosomal uptake of (model) drugs [39]. Furthermore, the observed trend is that endocytosis increases with an increase in acoustic pulse length and an increase in acoustic pressure amplitude. Surprisingly, even though the bubble oscillation amplitude of the 3.5-μm and the 4.7-μm bubbles was nearly identical at a PNP of 500 kPa, the bubbles with a radius of 4.7 μm resulted overall in a two times higher percentage of endocytic cells than those with a radius of 3.5 μm.

Regarding the measured sonoporation efficiencies (Figs. 4E and F), a similar and striking observation is made: in all cases that exceed the control values (Figs. 4E and F), the sonoporation efficiency is at least two times higher for the 4.7-μm bubbles as compared to that for the 3.5-μm bubbles. At a PNP of 250 kPa (Fig. 4E), only the 4.7-μm bubbles driven by the 1000-cycle pulse resulted in a sonoporation efficiency beyond the control value. Thus, even though both the 3.5-μm and the 4.7-μm bubbles oscillate on average with the same amplitude of oscillation when driven at a PNP of 500 kPa (see Fig. 3), the sonoporation efficiency of the 4.7-μm bubbles is substantially higher.

To further investigate the dependence of sonoporation efficiency on microbubble size, the sonoporation efficiency was quantified for a larger range of bubble radii, i.e., from 2.1 μm up to 6.2 μm (Fig. 2B). Here, the bubbles were driven only with the 1000-cycle pulse to induce a high degree of sonoporation. For the same reason, PNPs of 500 kPa and 750 kPa were selected. Additionally, to gain insight on the induced pore size, two FITC-dextran molecular weights were used (4 kDa and 2 MDa). All results are presented in Fig. 5. First, note that again, for all ultrasound settings the 4.7-μm bubbles resulted in the highest sonoporation efficiency. Upon an increase in PNP from 500 kPa to 750 kPa, the dependence of sonoporation efficiency on bubble size is maintained. Sonoporation efficiency of the smallest 2.1-μm bubbles is 5 to 30 times lower than that of the 4.7-μm bubbles. This large difference in sonoporation efficiency between small and large bubbles explains the on average 6 times lower sonoporation efficiency of the polydisperse bubble suspension as compared to the 4.7-μm bubbles. The broad polydisperse size distribution (see Fig. 2B) contains some of the efficient 4.7-μm bubbles, while the major part of all bubbles was even smaller than the less efficient 2.1-μm bubbles. Regarding the pore size, the results in Fig. 5 show that the surface concentration of pores large enough to allow the 2 MDa FITC-dextran molecules to diffuse into the cells doubles when the PNP is increased from 500 to 750 kPa. This observation is consistent with previous findings using polydisperse microbubbles [69]. All in all, for the present in vitro experiment using 1-MHz frequency ultrasound, sonoporation efficiency is at maximum for bubbles with a radius of 4.7 μm regardless of the molecular weight of the FITC model drug used here, and at a broad range of acoustic driving conditions: at 10, 100 and 1000 cycles and at acoustic pressure amplitudes of 250, 500 and 750 kPa.

If each bubble would sonoporate a single cell, a sonoporation efficiency of 7% would be reached (bubbles were diluted to approx. 1 bubble for every 15 cells). However, note that the sonoporation efficiencies at 500 kPa and 750 kPa at times exceed 7% meaning that bubbles must have moved across the cell monolayer to thereby porate multiple cells. Indeed, the supplementary high-speed recordings of monodisperse bubbles with a radius of 2.3, 4.0, and 6.0 μm show that bubble translation, coalescence, and size changes by diffusion also play a

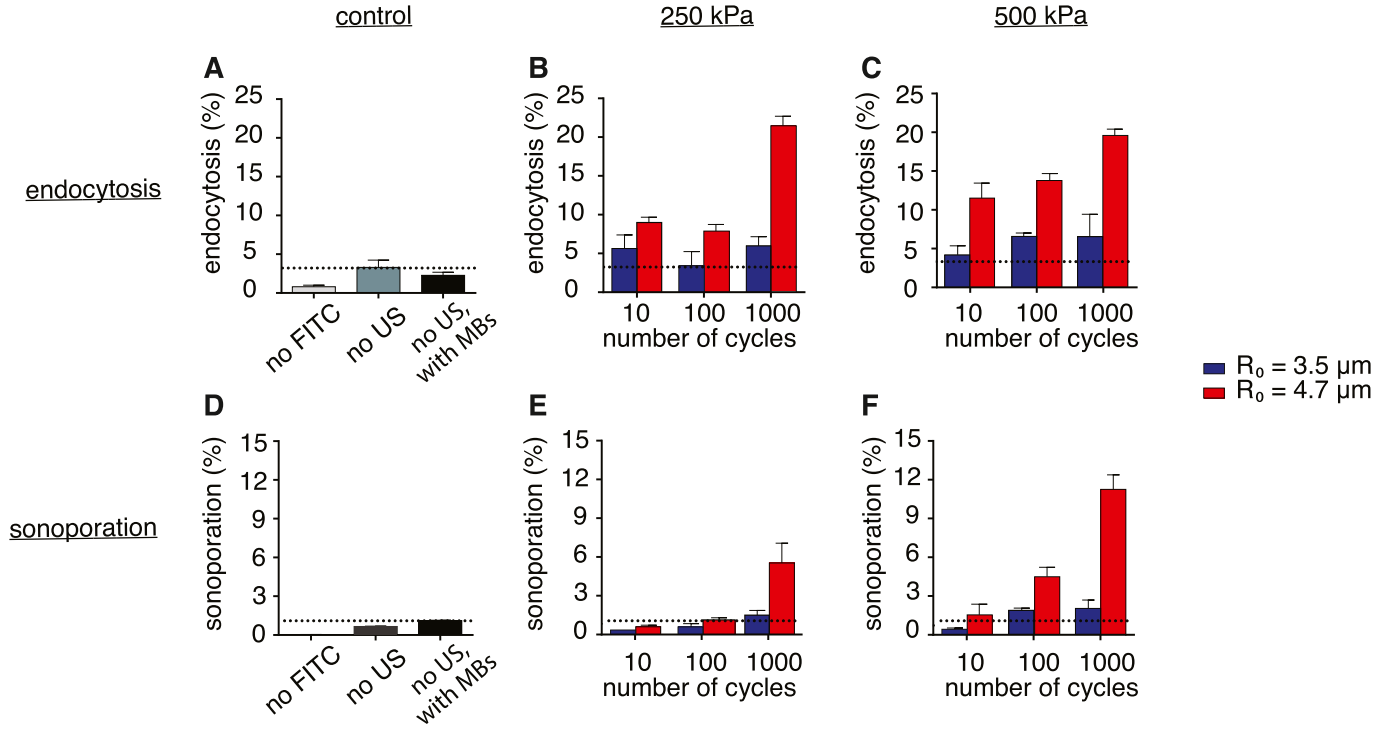

Fig. 4. (A,B,C) Endocytosis and (D,E,F) sonoporation efficiencies measured at PNPs of 250 kPa and 500 kPa for either 10, 100, or 1000-cycle pulses. The control experiments are shown in (A) and (D). The errorbars represent the standard error of the mean. To quantify sonoporation efficiency 2 MDa FITC-dextran was used. To discriminate between endocytosis and sonoporation, gating on the flow cytometry data was performed as in [39] and as illustrated in Fig. 2F.

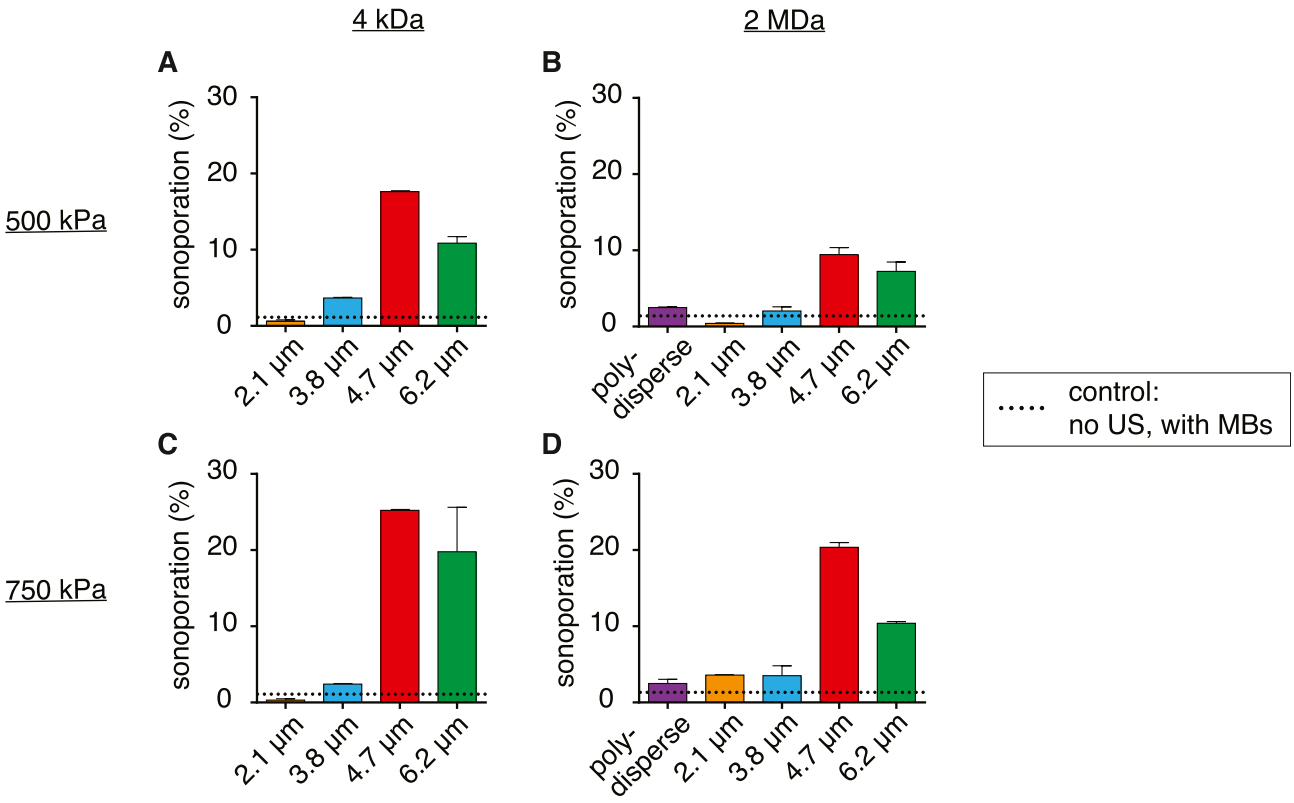

Fig. 5. Sonoporation efficiency at 1 MHz ultrasound driving frequency (1000 cycles) is at maximum for bubbles with a radius of 4.7 µm. This is demonstrated for both FITC dextrans of 4 kDa and 2 MDa, and for PNPs of 500 kPa and 750 kPa. The error bars represent the standard error of the mean.

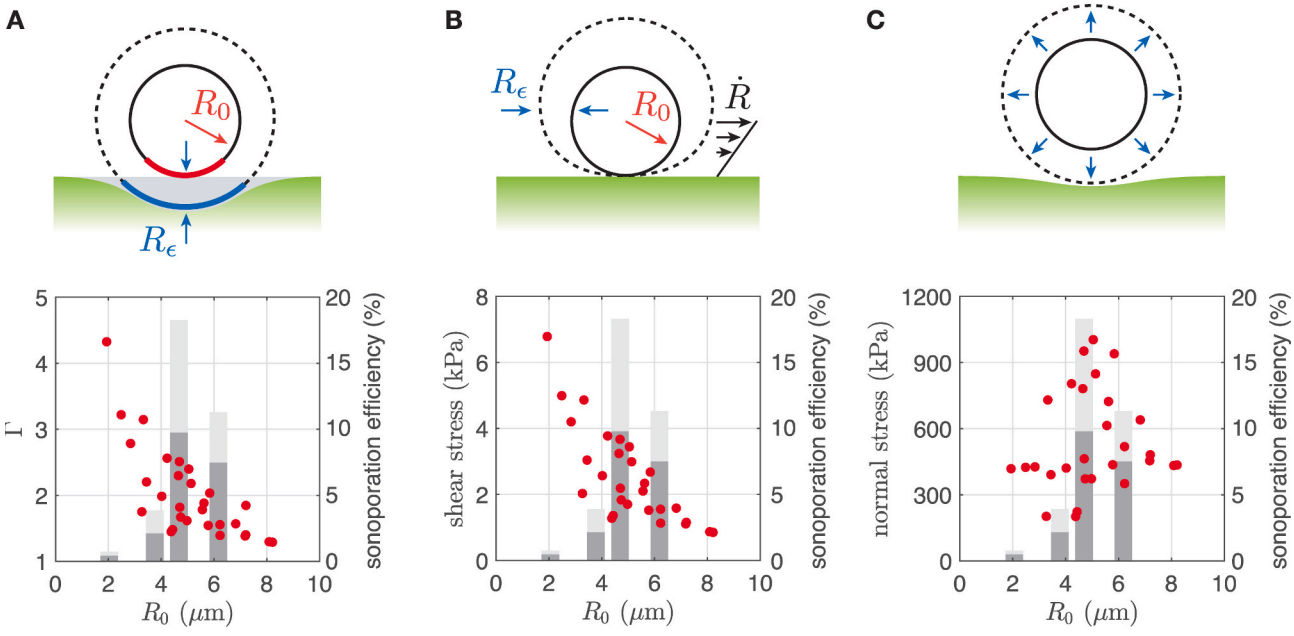

Fig. 6. Discussion on potential mechanisms of sonoporation. (A) If the cell (green shaded area) would be fluid like, its surface area dilatation Γ would follow that of the bubble. The plot shows that this assumption is incorrect as the maximum area increase of the bubble relative to its equilibrium surface area: $\Gamma = 4\pi(R_0 + \langle R_\epsilon \rangle)^2 / 4\pi R_0^2$ does not correlate to the bubble size dependence of the measured sonoporation efficiency. To aid comparison, the sonoporation efficiencies measured at 500 kPa and using 4 kDa and 2 MDa FITC-dextran are also plotted in light and dark gray, respectively. (B) Also the bubble size dependence of the estimated shear stress ($\tau = \mu \dot{R}/R_0$) does not correlate with that of the measured sonoporation efficiency. (C) Estimate of the normal stress exerted by the bubble on the cellular wall. Note that its bubble size dependence correlates well with that of the measured sonoporation efficiency suggesting that normal stress is the dominant mechanism of sonoporation in the present work. (For interpretation of the references to colour in this figure legend, the reader is referred to the web version of this article.)

role in sonoporation, in particular after tens of acoustic cycles (i.e., tens of microseconds). The recordings show that many of the 2.3-μm bubbles dissolve even before the end of the acoustic driving pulse. The 4.0 and 6.0-μm bubbles cluster within tens of μs after the arrival of the acoustic driving pulse. It is furthermore observed that the 6 μm bubbles shed off small bubbles after 285 μs. All these effects dramatically affect volumetric bubble oscillations and any subsequent mechanical effects on the cells. Thus, gaining understanding of sonoporation at driving pulses exceeding several tens of acoustic cycles is extremely challenging. Nevertheless, in this work we demonstrate that already at a pulse lengths of 10 cycles the sonoporation efficiency is strongly bubble size dependent and at maximum for bubbles approx. 4.7 μm in radius. Moreover, Fig. 4F shows that for the 4.7-μm bubbles driven at 500 kPa the sonoporation efficiency doubles each time the pulse length is increased by a factor 10. This weak dependence of sonoporation efficiency on pulse length (i.e., much weaker than linear) shows that most sonoporation is induced during the first cycles of the driving pulse, and thus before bubble translation, coalescence, and size changes play a role.

3.3. Discussion on potential mechanism(s) of sonoporation

We now discuss several potential physical mechanisms that can induce cell membrane dilation and thereby potentially cell membrane sonoporation. The scaling of the mechanisms with bubble size is compared to the measured sonoporation efficiency using the measured amplitude of oscillation (Fig. 3B).

We start by considering a most simple case, i.e., by assuming that the mechanical properties and strain of the cell follow a liquid-like behavior that equals that of the medium surrounding the cell. Under this assumption, cell membrane deformation directly follows from the radially diverging flow around an oscillating bubble. The surface area dilation of the cell membrane then scales as $\Gamma = 4\pi(R_0 + \langle R_\epsilon \rangle)^2 / 4\pi R_0^2$ (red and blue marked segments in Fig. 6A). In Fig. 6A Γ is plotted as a function of bubble size. The figure demonstrates that there is no correlation between Γ and the measured sonoporation efficiency. Thus, cell membrane dilation does not simply follow that of the bubble surface.

To couple bubble oscillations to cell membrane dilation, shear stresses τ (force per unit area parallel to the cell wall) due to streaming induced by the oscillating bubble has frequently been considered. Shear stress is defined as: $\tau = \mu \partial v/\partial z|_{z=0}$, with μ the liquid viscosity and $\partial v/\partial z|_{z=0}$ the fluid velocity gradient at and parallel to the cell wall. Due to the asymmetry induced by the nearby cell boundary the bubble induces next to periodic fluid velocity oscillations on the order of the bubble wall velocity (m/s), a net time averaged microstreaming flow (mm/s) [9,10,49]. As the time-averaged steady flow velocity is typically 3 orders of magnitude lower than the instantaneous oscillatory velocity of the bubble wall $\dot{R}$, we deem shear stress due steady microstreaming negligible as compared to non-steady shear stress. To estimate non-steady shear stress, the acoustic boundary layer thickness $\delta = \sqrt{2\mu(\rho\omega)^{-1}}$ is often used as the relevant length scale over which the bubble wall velocity $\dot{R}$ decays (i.e., $\partial v/\partial z \approx \dot{R}/\delta$) [11,70,71]. However, this is only the case for a bubble in the unbounded liquid oscillating at small amplitudes of oscillation ($\langle R_\epsilon \rangle \ll R_0$). In our experiments, the bubbles are located against a wall and their average bubble oscillation amplitude of typically 2–3 μm (see Fig. 2) is approximately 5 times lager than δ (0.56 μm). Therefore, we estimate the length scale over which $\dot{R}$ decays to be R_0 instead of δ (see the schematic in Fig. 6B) such that the shear stress is estimated as follows: $\tau = \mu \dot{R}/R_0$. The latter equation can then be linearized to find: $\tau \approx \mu\omega\langle R_\epsilon \rangle / R_0$. Fig. 6B shows the estimated shear stress τ based on the measured amplitude of bubble oscillations $\langle R_\epsilon \rangle$. The figure shows that the dependence of shear stress on bubble size does not correlate to the measured sonoporation efficiency. Thus, it is highly unlikely that shear stress is the relevant mechanism of sonoporation in the experiments presented here.

We now estimate the contribution of normal stresses (force per unit area perpendicular to the cell wall), which can also induce a lateral strain of the cell membrane. To estimate the normal stresses we start with Euler's equation in spherical coordinates: $\rho^{-1}\partial p/\partial r = -\partial v/\partial t - v\partial v/\partial r$, with ρ the liquid density, p the gauge pressure, and r the radial coordinate. Euler's equation can be integrated to obtain the well known expression for the pressure at the bubble wall relative to the ambient pressure [46,72]: $p = \rho\left(\ddot{R}R + \frac{3}{2}\dot{R}^2\right)$, which can in turn be linearized to obtain an estimate of the normal stress $p = \rho\omega^2\left(\langle R_\epsilon \rangle R_0 + \frac{3}{2}\langle R_\epsilon \rangle^2\right)$. Fig. 6C shows the estimated normal stress as a function of bubble size again calculated using the measured bubble oscillation amplitude $\langle R_\epsilon \rangle$. Note that the estimated normal stress is 2 to 3 orders of magnitude higher than the estimated shear stress and that it can exceed the driving acoustic pressure of 500 kPa. Also note that the estimated normal stress correlates well with the overall trend of the measured sonoporation efficiency. The exact relationship between normal stress, strain of the cell membrane, and the resulting sonoporation probability remains to be determined in future work. Nevertheless, if we consider a cell membrane to be an elastic membrane, its strain will be proportional to the applied stress. Therefore, the higher the stress, the larger the induced deformation, and the higher the chance of sonoporation. Thus, considering the three mechanisms discussed, normal stresses are most likely the dominant mechanism of sonoporation in the present work.

As to microjetting, the high-speed imaging experiments did not show any indications. In future work, the onset of microjetting, its role on sonoporation, and its dependency on bubble size remains to be determined, e.g., using sideview high-speed imaging. Additionally, the role of the full spectrum of frequencies contained in the bubble oscillations, i.e., fundamental response versus subharmonics and higher harmonics, remains to be determined. This work demonstrates that monodisperse microbubbles are a powerful tool in the search for such improved understanding. More toward the intended therapeutic application, this work demonstrates that sonoporation efficiency can be boosted by almost an order of magnitude when conventional UCAs are replaced by monodisperse bubble suspensions that are tailored to efficient sonoporation-based therapies. However, it is well known that bubble dynamics is influenced by the cell boundary and the confinement of the surrounding (viscoelastic) tissue [18,64,73], as such our 2D monolayer experiments cannot be directly translated to in-vivo conditions. The next step is to move to 3D organ-on-chip models [74], CAM models [75,76] and preclinical experiments [77].

4. Conclusions

Sonoporation induced by ultrasound with a frequency of 1 MHz is most efficiently induced by monodisperse microbubbles with a radius of 4.7 μm. By contrast, the sonoporation efficiency of bubbles with a 2.1-μm radius is approx. 40 times lower than that obtained with bubbles 4.7-μm in radius. Polydisperse microbubbles with a typical ultrasound contrast agent size distribution perform almost an order of magnitude lower in terms of sonoporation efficiency than the 4.7-μm bubbles. We furthermore demonstrate that the characteristic resonance behavior of microbubbles disappears for acoustic pressure amplitudes that induce sonoporation ($\geq$ 500 kPa) such that the bubble oscillation amplitude is approximately uniform across bubble radii ranging from 2 to 8 μm. It is shown that it is highly unlikely that shear stresses are driving the sonoporation mechanism in this system. Instead, we show that an estimate of the bubble-induced normal stresses correlates well with the measured sonoporation efficiency. This work therefore demonstrates that monodisperse microbubble suspensions are potentially improved therapeutic agents as well as a powerful tool in the search for an improved fundamental understanding of ultrasound-based bubble-mediated therapy.

Supplementary data to this article can be found online at https://doi.

org/10.1016/j.jconrel.2023.09.047.

CRediT authorship contribution statement

Benjamin van Elburg: Writing – review & editing, Writing – original draft, Visualization, Validation, Software, Methodology, Investigation, Formal analysis, Data curation. **Joke Deprez:** Writing – review & editing, Writing – original draft, Visualization, Validation, Methodology, Investigation, Formal analysis, Data curation. **Martin van den Broek:** Validation, Software, Methodology, Investigation, Formal analysis, Data curation, Visualization, Writing – review & editing. **Stefaan C. De Smedt:** Conceptualization, Funding acquisition, Project administration, Resources, Supervision, Writing – review & editing. **Michel Versluis:** Funding acquisition, Investigation, Methodology, Project administration, Resources, Supervision, Validation, Writing – review & editing. **Guillaume Lajoinie:** Funding acquisition, Investigation, Methodology, Supervision, Writing – review & editing. **Ine Lentacker:** Writing – review & editing, Visualization, Validation, Supervision, Resources, Project administration, Methodology, Investigation, Funding acquisition, Data curation, Conceptualization. **Tim Segers:** Writing – review & editing, Writing – original draft, Visualization, Validation, Supervision, Software, Resources, Project administration, Methodology, Investigation, Funding acquisition, Formal analysis, Data curation, Conceptualization.

Declaration of Competing Interest

None

Data availability

Data will be made available on request.

Acknowledgements

Ali Rezaei is acknowledged for his assistance in the preparation of the hydrogels. MvdB and TS acknowledge funding from the Max Planck Center Twente for Complex Fluid Dynamics. This work is partly funded by the Dutch research council (NWO, Ultra-X-Treme, P17-32). TS acknowledges funding from the European Union (ERC, MICOMAUS, 101078313).

References

[1] I. Lentacker, I. De Cock, R. Deckers, S. De Smedt, C. Moonen, Understanding ultrasound induced sonoporation: definitions and underlying mechanisms, Adv. Drug Deliv. Rev. 72 (2014) 49–64.
[2] K. Kooiman, S. Roovers, S.A. Langeveld, R.T. Kleven, H. Dewitte, M.A. O'Reilly, J.-M. Escoffre, A. Bouakaz, M.D. Verweij, K. Hynynen, et al., Ultrasound-responsive cavitation nuclei for therapy and drug delivery, Ultrasound Med. Biol. 46 (6) (2020) 1296–1325.
[3] J. Deprez, G. Lajoinie, Y. Engelen, S. De Smedt, I. Lentacker, Opening doors with ultrasound and microbubbles: beating biological barriers to promote drug delivery, Adv. Drug Deliv. Rev. 172 (2021) 9–36.
[4] J. Tu, A.C. Yu, Ultrasound-mediated drug delivery: sonoporation mechanisms, biophysics, and critical factors, BME Front. 2022 (2022).
[5] E. Stride, C. Coussios, Nucleation, mapping and control of cavitation for drug delivery, Nat. Rev. Phys. 1 (8) (2019) 495–509.
[6] A. van Wamel, K. Kooiman, M. Harteveld, M. Emmer, F.J. ten Cate, M. Versluis, N. de Jong, Vibrating microbubbles poking individual cells: drug transfer into cells via sonoporation, J. Control. Release 112 (2) (2006) 149–155.
[7] H. Chen, W. Kreider, A.A. Brayman, M.R. Bailey, T.J. Matula, Blood vessel deformations on microsecond time scales by ultrasonic cavitation, Phys. Rev. Lett. 106 (2011), 034301.
[8] P. Dayton, A. Klibanov, G. Brandenburger, K. Ferrara, Acoustic radiation force in vivo: a mechanism to assist targeting of microbubbles, Ultrasound Med. Biol. 25 (1999) 1195–1201.
[9] J.A. Rooney, Shear as a mechanism for sonically induced biological effects, J. Acoust. Soc. Am. 52 (6B) (1972) 1718–1724.
[10] P. Marmottant, S. Hilgenfeldt, Controlled vesicle deformation and lysis by single oscillating bubbles, Nature (2003) 153–156, https://doi.org/10.1038/nature01592.
[11] B. Helfield, X. Chen, S. Watkins, F. Villanueva, Biophysical insight into mechanisms of sonoporation, Proc. Natl. Acad. Sci. U. S. A. 113 (36) (2016) 9983–9988.
[12] S. Cleve, M. Guédra, C. Mauger, C. Inserra, P. Blanc-Benon, Microstreaming induced by acoustically trapped, non-spherically oscillating microbubbles, J. Fluid Mech. 875 (2019) 597–621.
[13] N. Mobadersany, K. Sarkar, Acoustic microstreaming near a plane wall due to a pulsating free or coated bubble: velocity, vorticity and closed streamlines, J. Fluid Mech. 875 (2019) 781–806.
[14] A. Prosperetti, A new mechanism for sonoluminescence, J. Acoust. Soc. Am. 101 (4) (1997) 2003–2007.
[15] P. Prentice, A. Cuschieri, K. Dholakia, M. Prausnitz, P. Campbell, Membrane disruption by optically controlled microbubble cavitation, Nat. Phys. 1 (2) (2005) 107–110.
[16] C.-D. Ohl, M. Arora, R. Ikink, N. De Jong, M. Versluis, M. Delius, D. Lohse, Sonoporation from jetting cavitation bubbles, Biophys. J. 91 (11) (2006) 4285–4295.
[17] S. Snipstad, E. Sulheim, C. de Lange Davies, C. Moonen, G. Storm, F. Kiessling, R. Schmid, T. Lammers, Sonopermeation to improve drug delivery to tumors: from fundamental understanding to clinical translation, Expert Opin. Drug Deliv. 15 (12) (2018) 1249–1261.
[18] B. Dollet, P. Marmottant, V. Garbin, Bubble dynamics in soft and biological matter, Annu. Rev. Fluid Mech. 51 (1) (2019) 331–355.
[19] I. Beekers, M. Vegter, K.R. Lattwein, F. Mastik, R. Beurskens, A.F. van der Steen, N. de Jong, M.D. Verweij, K. Kooiman, Opening of endothelial cell–cell contacts due to sonoporation, J. Control. Release 322 (2020) 426–438.
[20] I. Beekers, S.A. Langeveld, B. Meijlink, A.F. van der Steen, N. de Jong, M. D. Verweij, K. Kooiman, Internalization of targeted microbubbles by endothelial cells and drug delivery by pores and tunnels, J. Control. Release 347 (2022) 460–475.
[21] M. Eck, R. Aronovich, T. Ilovitsh, Efficacy optimization of low frequency microbubble-mediated sonoporation as a drug delivery platform to cancer cells, Int. J. Pharmaceut.: X 4 (2022) 100132.
[22] P. Marmottant, S. Van Der Meer, M. Emmer, M. Versluis, N. De Jong, S. Hilgenfeldt, D. Lohse, A model for large amplitude oscillations of coated bubbles accounting for buckling and rupture, J. Acoust. Soc. Am. 118 (6) (2005) 3499–3505.
[23] S. Roovers, T. Segers, G. Lajoinie, J. Deprez, M. Versluis, S.C. De Smedt, I. Lentacker, The role of ultrasound-driven microbubble dynamics in drug delivery: from microbubble fundamentals to clinical translation, Langmuir 35 (31) (2019) 10173–10191.
[24] M. Minnaert, On musical air-bubbles and the sound of running water, Philos. Mag. 16 (104) (1933) 235–248.
[25] P. Frinking, T. Segers, Y. Luan, F. Tranquart, Three decades of ultrasound contrast agents: a review of the past, present and future improvements, Ultrasound Med. Biol. 46 (4) (2020) 892–908.
[26] A.M. Gañán-Calvo, J.M. Gordillo, Perfectly monodisperse microbubbling by capillary flow focusing, Phys. Rev. Lett. 87 (2001) 274501.
[27] S.L. Anna, N. Bontoux, H.A. Stone, Formation of dispersions using "flow focusing" in microchannels, Appl. Phys. Lett. 82 (3) (2003) 364–366.
[28] P. Garstecki, I. Gitlin, W. DiLuzio, G.M. Whitesides, Formation of monodisperse bubbles in a microfluidic flow-focusing device, Appl. Phys. Lett. 85 (13) (2004) 2649–2651.
[29] K. Hettiarachchi, E. Talu, M.L. Longo, P.A. Dayton, A.P. Lee, On-chip generation of microbubbles as a practical technology for manufacturing contrast agents for ultrasonic imaging, Lab Chip 7 (4) (2007) 463–468.
[30] E. Talu, R.L. Powell, M.L. Longo, P.A. Dayton, Needle size and injection rate impact on microbubble contrast agent population, Ultrasound Med. Biol. 34 (7) (2008) 1182–1185.
[31] R. Shih, D. Bardin, D.T. Martz, P.S. Sheeran, P.A. Dayton, A.P. Lee, Flow-focusing regimes for accelerated production of monodisperse drug-loadable microbubbles toward clinical-scale applications, Lab Chip 13 (2013) 4816–4826.
[32] R. Shih, A.P. Lee, Post-formation shrinkage and stabilization of microfluidic bubbles in lipid solution, Langmuir 32 (8) (2016) 1939–1946.
[33] T. Segers, L. de Rond, N. de Jong, M. Borden, M. Versluis, Stability of monodisperse phospholipid-coated microbubbles formed by flow-focusing at high production rates, Langmuir 32 (16) (2016) 3937–3944.
[34] T. Segers, D. Lohse, M. Versluis, P. Frinking, Universal equations for the coalescence probability and long-term size stability of phospholipid-coated monodisperse microbubbles formed by flow-focusing, Langmuir 33 (39) (2017) 10329–10339.
[35] T. Segers, A. Lassus, P. Bussat, E. Gaud, P. Frinking, Improved coalescence stability of monodisperse phospholipid-coated microbubbles formed by flow-focusing at elevated temperatures, Lab Chip 19 (2019) 158–167.
[36] T. Segers, E. Gaud, G. Casqueiro, A. Lassus, M. Versluis, P. Frinking, Foam-free monodisperse lipid-coated ultrasound contrast agent synthesis by flow-focusing through multi-gas-component microbubble stabilization, Appl. Phys. Lett. 116 (17) (2020) 173701.
[37] N. Kudo, K. Okada, K. Yamamoto, Sonoporation by single-shot pulsed ultrasound with microbubbles adjacent to cells, Biophys. J. 96 (12) (2009) 4866–4876.
[38] A.R. Carson, C.F. McTiernan, L. Lavery, M. Grata, X. Leng, J. Wang, X. Chen, F. S. Villanueva, Ultrasound-targeted microbubble destruction to deliver siRNA cancer therapy, Cancer Res. 72 (23) (2012) 6191–6199.
[39] I. De Cock, E. Zagato, K. Braeckmans, Y. Luan, N. de Jong, S.C. De Smedt, I. Lentacker, Ultrasound and microbubble mediated drug delivery: acoustic pressure as determinant for uptake via membrane pores or endocytosis, J. Control. Release 197 (2015) 20–28.

[40] Y.C. Park, C. Zhang, S. Kim, G. Mohamedi, C. Beigie, J.O. Nagy, R.G. Holt, R. O. Cleveland, N.L. Jeon, J.Y. Wong, Microvessels-on-a-chip to assess targeted ultrasound-assisted drug delivery, ACS Appl. Mater. Interfaces 8 (46) (2016) 31541–31549.
[41] G. Silvani, C. Scognamiglio, D. Caprini, L. Marino, M. Chinappi, G. Sinibaldi, G. Peruzzi, M.F. Kiani, C.M. Casciola, Reversible cavitation-induced junctional opening in an artificial endothelial layer, Small 15 (51) (2019) 1905375.
[42] K.R. Lattwein, I. Beekers, J.J. Kouijzer, M. Leon-Grooters, S.A. Langeveld, T. van Rooij, A.F. van der Steen, N. de Jong, W.J. van Wamel, K. Kooiman, Dispersing and sonoporating biofilm-associated bacteria with sonobactericide, Pharmaceutics 14 (6) (2022) 1164.
[43] L.A. Crum, Bjerknes forces on bubbles in a stationary sound field, J. Acoust. Soc. Am. 57 (6) (1957) 1363–1370.
[44] T.J.A. Kokhuis, B.A. Naaijkens, L.J.M. Juffermans, O. Kamp, A.F.W. van der Steen, M. Versluis, N. de Jong, On the dynamics of stembells: microbubble-conjugated stem cells for ultrasound-controlled delivery, Appl. Phys. Lett. 111 (2) (2017), 023701.
[45] P.S. Epstein, M.S. Plesset, On the stability of gas bubbles in liquid-gas solutions, J. Chem. Phys. 18 (11) (1950) 1505–1509.
[46] T.G. Leighton, The Acoustic Bubble, Academic Press, 1994.
[47] J. O'Brien, N. Ovenden, E. Stride, Accounting for the stability of microbubbles to multi-pulse excitation using a lipid-shedding model, J. Acoust. Soc. Am. 130 (2011) 180–185.
[48] Y. Luan, G. Lajoinie, E. Gelderblom, I. Skachkov, A.F.W. van der Steen, H.J. Vos, M. Versluis, N. de Jong, Lipid shedding from single oscillating microbubbles, Ultrasound Med. Biol. 40 (8) (2014) 1834–1846.
[49] G. Lajoinie, Y. Luan, E. Gelderblom, B. Dollet, F. Mastik, H. Dewitte, I. Lentacker, N. de Jong, M. Versluis, Non-spherical oscillations drive the ultrasound-mediated release from targeted microbubbles, Commun. Phys. 1 (2018) 22.
[50] Z. Fan, R. Kumon, C. Deng, Mechanisms of microbubble-facilitated sonoporation for drug and gene delivery, Ther. Deliv. 5 (2014) 467–486, https://doi.org/10.4155/tde.14.10.
[51] E. Gelderblom, F. Wolbers, N. De Jong, A. Van den Berg, M. Versluis, Time-resolved high-speed fluorescence imaging of bubble-induced sonoporation, Proceed. Meet. Acoust. 19 (1) (2013) 075070.
[52] K. Kooiman, M. Foppen-Harteveld, A.F. van der Steen, N. de Jong, Sonoporation of endothelial cells by vibrating targeted microbubbles, J. Control. Release 154 (1) (2011) 35–41.
[53] I. De Cock, G. Lajoinie, M. Versluis, S.C. De Smedt, I. Lentacker, Sonoprinting and the importance of microbubble loading for the ultrasound mediated cellular delivery of nanoparticles, Biomaterials 83 (2016) 294–307.
[54] G. Lajoinie, I. De Cock, C.C. Coussios, I. Lentacker, S. Le Gac, E. Stride, M. Versluis, In vitro methods to study bubble-cell interactions: fundamentals and therapeutic applications, Biomicrofluidics 10 (1) (2016), 011501.
[55] B.D. Meijering, L.J. Juffermans, A. van Wamel, R.H. Henning, I.S. Zuhorn, M. Emmer, A.M. Versteilen, W.J. Paulus, W.H. van Gilst, K. Kooiman, et al., Ultrasound and microbubble-targeted delivery of macromolecules is regulated by induction of endocytosis and pore formation, Circ. Res. 104 (5) (2009) 679–687.
[56] T. Segers, E. Gaud, M. Versluis, P. Frinking, High-precision acoustic measurements of the non-linear dilatational elasticity of phospholipid coated monodisperse microbubbles, Soft Matter 14 (2018) 9550.
[57] B. van Elburg, G. Collado-Lara, G.-W. Bruggert, T. Segers, M. Versluis, G. Lajoinie, Feedback-controlled microbubble generator producing one million monodisperse bubbles per second, Rev. Sci. Instrum. 92 (3) (2021), 035110.
[58] T. Segers, N. de Jong, M. Versluis, Uniform scattering and attenuation of acoustically sorted ultrasound contrast agents: modeling and experiments, J. Acoust. Soc. Am. 140 (4) (2016) 2506–2517.
[59] Z. Imam, Importance of Viscosity in Cell Culture Media. https://blog.rheosense.com/importance-of-viscosity-in-cell-culture-media, 2020 [Retrieved 27 March, 2023].
[60] K. Braeckmans, L. Peeters, N.N. Sanders, S.C. De Smedt, J. Demeester, Three-dimensional fluorescence recovery after photobleaching with the confocal scanning laser microscope, Biophys. J. 85 (4) (2003) 2240–2252.
[61] T. Segers, M. Versluis, Acoustic bubble sorting for ultrasound contrast agent enrichment, Lab Chip 14 (10) (2014) 1705–1714.
[62] A.H. Negussie, A. Partanen, A.S. Mikhail, S. Xu, N. Abi-Jaoudeh, S. Maruvada, B. J. Wood, Thermochromic tissue-mimicking phantom for optimisation of thermal tumour ablation, Int. J. Hyperth. 32 (3) (2016) 239–243.
[63] M. Usumura, R. Kishimoto, K. Ishii, E. Hotta, J. Kershaw, T. Higashi, T. Obata, M. Suga, Longitudinal stability of a multimodal visco-elastic polyacrylamide gel phantom for magnetic resonance and ultrasound shear-wave elastography, PLoS One 16 (2021), e0250667, https://doi.org/10.1371/journal.pone.0250667.
[64] M. Versluis, E. Stride, G. Lajoinie, B. Dollet, T. Segers, Ultrasound contrast agent modeling: a review, Ultrasound Med. Biol. 46 (9) (2020) 2117–2144.
[65] V. Garbin, D. Cojoc, E. Ferrari, E. Di Fabrizio, M. Overvelde, S. Van Der Meer, N. De Jong, D. Lohse, M. Versluis, Changes in microbubble dynamics near a boundary revealed by combined optical micromanipulation and high-speed imaging, Appl. Phys. Lett. 90 (11) (2007) 114103.
[66] A.A. Doinikov, L. Aired, A. Bouakaz, Acoustic scattering from a contrast agent microbubble near an elastic wall of finite thickness, Phys. Med. Biol. 56 (21) (2011) 6951.
[67] T.A. Hay, Y.A. Ilinskii, E.A. Zabolotskaya, M.F. Hamilton, Model for bubble pulsation in liquid between parallel viscoelastic layers, J. Acoust. Soc. Am. 132 (1) (2012) 124–137.
[68] A.A. Doinikov, A. Bouakaz, Interaction of an ultrasound-activated contrast microbubble with a wall at arbitrary separation distances, Phys. Med. Biol. 60 (20) (2015) 7909–7925.
[69] F. Yang, N. Gu, D. Chen, X. Xi, D. Zhang, Y. Li, J. Wu, Experimental study on cell self-sealing during sonoporation, J. Control. Release 131 (3) (2008) 205–210.
[70] K. Kooiman, H.J. Vos, M. Versluis, N. de Jong, Acoustic behavior of microbubbles and implications for drug delivery, Adv. Drug Deliv. Rev. 72 (2014) 28–48.
[71] A. van Wamel, M. MŘhlenpfordt, R. Hansen, A. Healey, F.S. Villanueva, S. Kotopoulis, C. de Lange Davies, X. Chen, Ultrafast microscopy imaging of acoustic cluster therapy bubbles: activation and oscillation, Ultrasound Med. Biol. 48 (9) (2022) 1840–1857.
[72] K. Vokurka, On Rayleigh's model of a freely oscillating bubble. 1. Basic relations, Czechoslov. J. Phys. 35 (1) (1985) 28–40.
[73] B. Helfield, J.J. Black, B. Qin, J. Pacella, X. Chen, F.S. Villanueva, Fluid viscosity affects the fragmentation and inertial cavitation threshold of lipid-encapsulated microbubbles, Ultrasound Med. Biol. 42 (3) (2016) 782–794.
[74] R. Mittal, F.W. Woo, C.S. Castro, M.A. Cohen, J. Karanxha, J. Mittal, T. Chhibber, V.M. Jhaveri, Organ-on-chip models: implications in drug discovery and clinical applications, J. Cell. Physiol. 234 (6) (2019) 8352–8380.
[75] T. Faez, M. Emmer, K. Kooiman, M. Versluis, A.F. van der Steen, N. de Jong, 20 years of ultrasound contrast agent modeling, IEEE Trans. Ultrason. Ferroelec. Freq. Contr. 60 (1) (2012) 7–20.
[76] E. Pion, J. Karnosky, S. Boscheck, B.J. Wagner, K.M. Schmidt, S.M. Brunner, H. J. Schlitt, T. Aung, C. Hackl, S. Haerteis, 3D in vivo models for translational research on pancreatic cancer: the chorioallantoic membrane (CAM) model, Cancers 14 (15) (2022) 3733.
[77] S. Snipstad, S. Hanstad, A. Bjørkøy, Ý. Mørch, C. de Lange Davies, Sonoporation using nanoparticle-loaded microbubbles increases cellular uptake of nanoparticles compared to co-incubation of nanoparticles and microbubbles, Pharmaceutics 13 (5) (2021) 640.